OH mid-infrared emission as a diagnostic of H2O UV photodissociation: II. Application to interstellar photodissociation regions

Zannese, M.; Tabone, B.; Habart, E.; Le Petit, F.; Dishoeck, E.F. van; Bron, E.

Astronomy & Astrophysics

OH mid-infrared emission as a diagnostic of H₂O UV photodissociation

II. Application to interstellar photodissociation regions

M. Zannese[1], B. Tabone[1], E. Habart[1], F. Le Petit[2], E. F. van Dishoeck[3,4], and E. Bron[2]

[1] Université Paris-Saclay, CNRS, Institut d'Astrophysique Spatiale, 91405 Orsay, France
e-mail: marion.zannese@universite-paris-saclay.fr
[2] LERMA, Observatoire de Paris, PSL Research University, CNRS, Sorbonne Université, 92190 Meudon, France
[3] Leiden Observatory, Leiden University, 2300 RA Leiden, The Netherlands
[4] Max-Planck Institut für Extraterrestrische Physik (MPE), Giessenbachstr. 1, 85748 Garching, Germany

ABSTRACT

Context. Water photodissociation in the 114–143 nm UV range forms excited OH which emits at mid-infrared (MIR) wavelengths via highly excited rotational lines. These lines have only been detected with *Spitzer* in proto-planetary disks and shocks. Previous studies have shown that they are a unique diagnostic for water photodissociation. Thanks to its high sensitivity and angular resolution, the *James Webb* Space Telescope (JWST) could be able to detect them in other environments such as interstellar photodissociation regions (PDRs).
Aims. Our goal is to predict OH MIR lines for a large range of thermal pressures and UV fields in PDRs.
Methods. We use the Meudon PDR Code to compute the thermal and chemical structure of PDRs. In order to predict the emerging spectrum of OH, we amended the code to include prompt emission induced by H₂O photodissociation between 114 and 143 nm. We performed a detailed study of the influence of thermal pressure ($P_{th}/k = n_H T_K$) and UV field strength on the integrated intensities and their detectability with the JWST.
Results. OH MIR emission is predicted to originate very close to the H^0/H₂ transition and is directly proportional to the column density of water photodissociated in that layer. Because gas-phase neutral–neutral reactions forming water require relatively high temperatures ($T_K \gtrsim 300$ K), the resulting OH MIR lines are primarily correlated with the temperature at this position, and are therefore brighter in regions with high pressure. This implies that these lines are predicted to be only detectable in strongly irradiated PDRs ($G_0^{incident} > 10^3$) with high thermal pressure ($P_{th}/k \gtrsim 5 \times 10^7$ K cm^{-3}). In the latter case, OH MIR lines are less dependent on the strength of the incident UV field. The detection of such lines in PDRs such as the Orion bar – which should be possible – is also investigated and we show that the line-to-continuum ratio could be a major limitation for detection because of instrumental limitations.
Conclusions. OH MIR lines observable by JWST are a promising diagnostic for dense and strongly irradiated PDRs and proplyds. Their intensities are directly proportional to the amount of water photodissociated and they are therefore an indirect but sensitive probe of the gas temperature at the H^0/H₂ transition.

Key words. photon-dominated region – ISM: molecules – molecular processes – astrochemistry – stars: formation – infrared: ISM

1. Introduction

Photodissociation regions (PDRs) are places where radiative feedback is dominant, with intense stellar far-ultraviolet (FUV) radiation playing a dominant role in the physics and chemistry (for a review, see e.g., Hollenbach & Tielens 1999; Wolfire et al. 2022). Stellar feedback is one of the major mechanisms that limit star formation (e.g., Inoguchi et al. 2020) by contributing to dispersal of the cloud due to gas heating and addition of angular momentum. Studying these regions is therefore essential in order to gain a better understanding of star formation and evolution of the interstellar matter. As a consequence of the intense UV field (up to a few 10^5 in units of the Mathis field corresponding to 1.9×10^{-3} erg s^{-1} cm^{-2}, Mathis et al. 1983), PDRs act as a cradle of very active chemistry, which is even more enhanced in dense star forming regions (with densities of around $n_H \sim 10^6$ cm^{-3}). Moreover, emission from PDRs, which reprocess a significant part of the radiation energy emitted by

young stars, dominates the infrared (IR) spectra from the galaxies in which they are located. It is therefore crucial to understand how the observed mid-infrared (MIR) emission is linked with physical conditions, and how these observations can constrain astrophysical environments.

The study of interstellar PDRs, such as the Orion Bar, NGC 7023, or the Horsehead nebula, is also important for understanding the still unknown UV-driven processes in other interstellar and circumstellar media. Observations and models of planetary nebulae indicate that a large fraction of the gas ejected by evolved stars goes through a PDR phase before being injected into the interstellar medium (ISM; Hollenbach & Natta 1995; Bernard-Salas & Tielens 2005). Infrared spectroscopy can provide information on the initial physical and chemical properties of the PDR phase (e.g., Bernard-Salas et al. 2009; Cox et al. 2016) and probe the photo-chemical evolution of molecules, nanoparticles, and grains. Dense and highly irradiated PDRs are also present in the FUV-illuminated surfaces of protoplanetary

disks (e.g., Visser et al. 2007; Woitke et al. 2009). In summary, PDRs are present in a wide variety of environments and the interstellar PDRs represent a unique laboratory for use in studying UV-driven micro-processes.

Because of the layered structure with a strong variation of physical conditions across the PDR, a multi-wavelength study is needed to trace every zone. Emission lines with high upper-level energy from atomic ions (e.g., S^+, Si^+, Fe^+, Kaufman et al. 2006) trace the ionization front. Ro-vibrational and pure rotational lines of H_2 (e.g., Parmar et al. 1991; Luhman et al. 1994; van der Werf et al. 1996; Walmsley et al. 2000; Allers et al. 2005; Habart et al. 2005, 2011; Sheffer et al. 2011; Kaplan et al. 2017; Zhang et al. 2021) probe the H^0/H_2 dissociation front. Slightly further into the PDRs, the excited molecular gas is traced by rotationally excited lines from species such as CO (e.g., Stutzki & Guesten 1990; Tauber et al. 1994; Hogerheijde et al. 1995; Nagy et al. 2017; Joblin et al. 2018; Parikka et al. 2018), CH^+, or OH (e.g., Goicoechea et al. 2011; Parikka et al. 2017). Key PDR signatures in the IR also include aromatic bands and dust continuum emission (e.g., Tielens 1993; Compiègne et al. 2011; Schirmer et al. 2020).

In order to spatially resolve the scale of FUV photon penetration (i.e., $A_V \sim 1$) in dense molecular clouds, high-angular-resolution observations are needed. For instance, observations with the Atacama Large Millimeter/submillimeter Array (ALMA) with a spatial resolution of 1" reveal a very complex structure at the interface of the molecular cloud and the ionized gas for the highly illuminated Orion Bar PDR rather than a homogenous layered structure (Goicoechea et al. 2016). Moreover, recent near-infrared (NIR) *Keck*/NIRC2 observations with a resolution of ~0.1" resolved the substructures of this interface – especially at the H^0/H_2 transition – revealing several ridges and extremely sharp filaments (Habart et al. 2022). We observe a spatial coincidence between the H_2 1–0 S(1) vibrational and HCO^+ $J = 4$–3 rotational emission previously obtained with ALMA. This highlights the fact that in high-pressure PDRs, the H^0/H_2 and C^+/C^0/CO transition zones almost coincide and are closer than expected for a typical layered structure of a constant-density PDR. The need for angular resolution is even more important in order to resolve these two spatially close transitions.

Up to now, the spatial resolution attained in the MIR domain (by *Spitzer*, *ISO*, etc.) has been insufficient to resolve the sharp transition between hot ionized diffuse gas and cold molecular dense gas. The upcoming *James Webb* Space Telescope (JWST) observations will improve our understanding of these regions as this instrument will provide new data in the IR wavelengths between 0.6 and 28.8 μm. In particular, the MIRI instrument of the JWST, observing in the MIR, will combine high-angular-resolution maps (up to 0.2") and IFU spectroscopy giving access to spatially resolved spectra at each pixel of the map; its high sensitivity will also enable the detection of numerous weak lines. Overall, the JWST observations will allow the warm and hot gas to be traced at small spatial scales, shedding new light on the FUV-driven chemistry and the physical conditions in these regions. In particular, a well-observed highly illuminated PDR, the Orion Bar, will be the target of an Early Release Science (ERS) program PDRs4All (1288) with the JWST (Berné et al. 2022) and a Guaranteed Time Observations (GTO) program "Physics and Chemistry of PDR Fronts" (1192) will focus on the Horsehead nebula and NGC-7023.

Among all the different lines in the MIR, the rotationally excited OH lines in the $\lambda = 9$–15 μm range appear the most promising diagnostic to unveil UV-driven processes in PDRs. Indeed, the incident UV field on the cloud leads to H_2O

photodissociation that produces mostly OH with various quantum states. Interestingly, when photodissociation is caused by short-wavelength photons ($114 \le \lambda \le 143$ nm, i.e., via the $\tilde{B}$ state of H_2O), OH is formed in highly rotationally excited states (~40 000 K, corresponding to $N > 35$; van Harrevelt & van Hemert 2000). The subsequent de-excitation of these nascent OH products via a radiative cascade produces MIR lines, a process called "prompt emission". Further modeling with a single-zone model shows that the line fluxes give unique access to the amount of water photodissociated per unit of time (Tabone et al. 2021). Therefore, in PDRs, MIR OH lines could be a unique diagnostic with which to constrain the physical conditions that affect the amount of water that is photodissociated there: typically the temperature at the H^0/H_2 transition. Although previous studies have derived H_2O column densities using emission lines observed by *Herschel* (e.g., Choi et al. 2014; Putaud et al. 2019), those data mostly probe the cold regions of the PDR where H_2O is very weakly photodissociated. Therefore, these latter results give access to different constraints from those provided by OH MIR emission. However, up to now, these rotationally excited lines of OH have only been detected with *Spitzer* in protoplanetary disks and strong protostellar shocks (e.g., Tappe et al. 2008, 2012; Najita et al. 2010; Carr & Najita 2014). In PDRs and proplyds, only less excited FIR lines of OH ($E_u/k \sim 100$–300 K) – which are more likely to be excited by collisions – have been detected (e.g., Goicoechea et al. 2011; Parikka et al. 2018). Therefore, investigating the detectability and the potential of MIR lines of OH in PDRs requires the use of detailed modeling.

In this paper, we predict OH MIR line intensities in PDRs by computing the chemistry, thermal balance, and excitation of OH in a consistent way using the Meudon PDR code. We then study how the key physical parameters of a PDR – which in our modeling framework are the thermal pressure and the strength of the incident UV field – affect the intensities. The paper is organized as follows. In Sect. 2, we summarize the main ingredients of the Meudon PDR code and the updates made to model OH prompt emission. In Sect. 3, we present our main results for H_2O and OH chemistry and the resulting MIR OH lines for a grid of models. In Sect. 4, our model is applied to the Orion Bar where we discuss their detectability with JWST, taking into account continuum, bands, and other lines. Finally, we discuss the detectability of MIR OH lines in other environments. Our findings are summarized in Sect. 5.

2. Models

2.1. Thermo-chemical model with the Meudon PDR Code

In this work, we computed H_2O and OH density profiles and the local UV field intensity as a function of the depth into the PDR using the Meudon PDR code (version 1.5.4[1], Le Petit et al. 2006). The code simulates the thermal and chemical structure of the gas in a self-consistent manner, considering a 1D geometry and a stationary state in a plane-parallel irradiated gas and dust layer. This code takes the shape of the incident UV field as input. Here, we use the Mathis et al. (1983) prescription for the grid of models (see Sect. 3), and a radiation field representative of an O7 star for our application to the Orion Bar (see Sect. 4). The code includes the progressive attenuation of the UV field due to grain and gas extinction. In this work, we use a

---

[1] Public version of August 2021: `https://pdr.obspm.fr/pdr_download.html`

mean galactic extinction curve with the parameterization of Fitzpatrick & Massa (1988) for the grid of models (see Sect. 3) and a flatter extinction curve for the Orion Bar (see Sect. 4 for further details). The chemistry of the PDR is computed taking into account hundreds of species and thousands of chemical reactions. The excitation of the several key species is considered in the calculation of the thermal balance as the cooling relies on line emission. The photoelectric effect and thermal coupling between gas and dust are also taken into account in the thermal balance.

In this paper, we assume that the PDR is isobaric. This is an appropriate starting hypothesis given that several studies show that isobaric models reproduce the observed emission of warm molecular gas in interstellar PDRs such as the Horsehead, NGC-7023, and the Orion Bar (e.g., Habart et al. 2005; Allers et al. 2005; Joblin et al. 2018). However, magnetic and turbulence pressure may be important in PDRs (e.g., van Dishoeck & Black 1986; Pellegrini et al. 2009; Pabst et al. 2020) and the thermal pressure might not dominate. For instance, in the Orion Bar, the nonthermal turbulent pressure is of the same order as the gas thermal pressure (see Table 1 of Goicoechea et al. 2016). Consequently, the density and temperature gradients calculated in isobaric models may not fully fit the gas structure of a PDR. However, in order to estimate the emission of MIR OH lines and investigate how it varies with the excitation and physical conditions (i.e., temperature and density), this assumption is valid as a first approximation. This study is based on a grid of models with thermal pressure ranging from $P_{\text{th}}/k = 10^5$ to 10^9 K cm^{-3} ($P_{\text{th}}/k = n_{\text{H}} T_{\text{K}}$) and an intensity of the FUV field from $G_0^{\text{incident}} = 10^2$ to 10^5 in units of the interstellar radiation field of Mathis et al. (1983). All the parameters fed into the models are summarized in Table 1. A fiducial model with $P_{\text{th}}/k = 10^8$ K cm^{-3} and $G_0^{\text{incident}} = 10^4$ (typical parameters of highly excited PDRs such as the Orion Bar) is adopted to present the results. In the following paragraphs, we review the microphysical processes that are key for the modeling of the warm molecular layer where OH MIR emission originates.

In the Meudon PDR Code, the H$_2$ rotational and rovibrational levels are calculated including collisional (de-)excitation with H (Wrathmall & Flower 2007), He, H$_2$ (Flower & Roueff 1998, 1999) and H$^+$, and UV radiative pumping of electronic lines followed by fluorescence. For our grid of models, we use the FGK approximation (Federman et al. 1979), which allows rapid computation for the UV radiative transfer involving self-shielding effects. The levels of H$_2$ are also populated considering excitation due to formation on grain surfaces. For the formation on dust surfaces, we assume a Boltzmann distribution at a temperature of one-third of H$_2$ dissociation energy (Black & van Dishoeck 1987). As the branching ratio of the distribution of H$_2$ dissociation energy is unknown because it probably depends on conditions in the PDR and the nature of the grains, it is assumed that distribution follows an equipartition law. The two remaining thirds of H$_2$ formation energy are distributed between grain excitation and the kinetic energy of released molecules.

The version of the code used in this paper includes an extensive chemical network. However, H$_2$O molecule formation is computed only taking into account the gas-phase chemistry, and the formation on grains is neglected. As this study focuses on the photodissociation of water in warm regions, the only formation mechanism of interest here is gas-phase formation, so it does not affect the results. Chemical reaction rates are computed using thermal rate coefficients, except for the formation of CH$^+$, SH$^+$, OH, and H$_2$O. For instance, a state-specific chemistry is included for the formation of OH and H$_2$O as a result

Table 1. Input parameters of the Meudon PDR code.

Parameters	Values
A_V^{tot}	20
P_{th}/k (K cm^{-3})	10^5–10^6–10^7–**10^8**–10^9
G_0^{incident} (Mathis unit)	10^2–10^3–**10^4**–10^5
Transfer	**FGK approximation**
Cosmic rays (s^{-1} per H$_2$)	5×10^{-17}
R_V	3.1
N_{H}/E(B-V) (cm^{-2})	5.8×10^{21}
Dust to gas ratio	0.01
Grain size distribution	$\propto \alpha^{-3.5}$
Min grain radius (cm)	1×10^{-7}
Max grain radius (cm)	3×10^{-5}

of reactions with H$_2$ with an energy barrier (see further details in Sect. 3.1.1 with Eqs. (3) and (4)). This allows the internal energy of H$_2$ to be considered in the rate coefficient and this energy may be used to overcome an activation barrier. Regarding the reaction OH + H$_2(v, J)$, the state-specific chemistry is taken into account by replacing the activation energy by the difference between the activation energy and the ro-vibrational energy of H$_2$ (e.g. Tielens & Hollenbach 1985a; Sternberg & Dalgarno 1995). This approach may not be fully accurate. However, the state-specific rate coefficients of the reaction OH + H$_2(v)$ are unknown except for $v = 1$ (Zellner & Steinert 1981; Zhang & Zhang 1994; Truong 1995). This approximation gives coherent results with the state-specific rate coefficient determined in these latter studies. Moreover, when this approximation is not adopted and only the thermal rate coefficient is used, the abundance of H$_2$O is reduced by a factor of three. We expect the true value of the abundance to be between these two limits. Therefore, this assumption is valid as a first approximation. Regarding the reaction O + H$_2$, we amended the version of the Meudon PDR code used in this paper to include the H$_2(v, J)$ state-specific rate coefficients recently computed by Veselinova et al. (2021). The H$_2$O and OH photodissociation rates are consistently computed by integrating the cross section over the local radiation field using the compiled cross section from the Leiden database (Heays et al. 2017).

2.2. Excitation of OH

The OH excitation was computed in concert with the chemistry and the thermal balance using the method of Gonzalez Garcia et al. (2008), which takes into account radiative pumping and collisional excitation, and allows us to include the formation of species in excited states. In order to include the impact of OH production in rotationally excited states, we assume that only H$_2$O photodissociation in the 114–143 nm UV range leads to the production of OH with a nonthermal state distribution and that the destruction pathways are not state-specific; that is, the destruction rate of an OH molecule is independent of its state. Any other formation route but H$_2$O photodissociation in the 114–143 nm range is assumed to produce OH with a thermal state distribution at the local temperature of the gas. Therefore, we neglected prompt emission of OH induced by water photodissociation at longer wavelength, which produces vibrationally hot but rotationally cold OH (van Harrevelt & van Hemert 2001), and chemical pumping by O+H$_2$, which produces OH in lower

rotational states $N < 25$ (Liu et al. 2000, and A. Zanchet, priv. comm.). These excitation processes do not impact the highly rotationally excited lines of OH in the 9–15 µm range, which are the focus of the present study (see discussion in Tabone et al. 2021).

These assumptions lead to the detailed balance equation:

$$\sum_{j \neq i} P_{ji} n_j - n_i \sum_{j \neq i} P_{ij} + F_{\mathrm{pd}} \bar{f}_i + (F - F_{\mathrm{pd}}) f_i(T_K) - F \frac{n_i}{n(\mathrm{OH})} = 0, \tag{1}$$

where n_i [cm^{-3}] is the local population density of OH at a given position in the PDR. P_{ij} are the radiative and collisional transition probabilities and include the contribution of the line and dust emission to the local radiation field (see Gonzalez Garcia et al. 2008, for further details). We considered collisional (de-)excitation of OH with He and H_2 using collisional rate coefficients of Kłos et al. (2007) and Offer et al. (1994), which have been further extrapolated to include collisional transitions between higher rotational levels of OH as in Tabone et al. (2021). F is the total formation rate of OH and $f_i(T_K)$ is the Boltzmann distribution at a temperature T_K. Also, F_{pd} is the production rate of OH via H_2O photodissociation in the 114–143 nm band [cm^{-3}s^{-1}] as defined by

$$F_{\mathrm{pd}} = n_{H_2O} \int_{114\,\mathrm{nm}}^{143\,\mathrm{nm}} \sigma(\lambda) I(\lambda) \mathrm{d}\lambda, \tag{2}$$

where $\sigma(\lambda)$ is the photodissociation cross section of H_2O, $I(\lambda)$ is the local UV radiation field, and n_{H_2O} is the local number density of H_2O. Finally, $\bar{f}_i$ in Eq. (1) is the state distribution of OH following H_2O photodissociation. The exact distribution $\bar{f}_i$ produced by water photodissociation in the 114–143 nm UV range depends relatively weakly on the shape of the local radiation field, and in this work we adopt the distribution produced by Lyman-α photons ($\lambda = 121.6$ nm) presented in Tabone et al. (2021).

Following Tabone et al. (2021), our OH model includes the list of energy levels and radiative transitions provided by Brooke et al. (2016). In order to reduce the computational time, the number of OH levels has been reduced to a total of 412 by limiting the vibrational quantum number to $v \leq 1$ and including only the OH(X) electronic ground state. All the rotational levels that are stable within a vibrational state are retained, which corresponds to $N \leq 50$ and $N \leq 48$ for $v = 0$ and 1, respectively. In order to account for prompt emission induced by the production of OH in the levels that have been discarded, we use the reduced-state distribution $\bar{f}_i$ derived by Tabone et al. (in prep.). Each rotational level is further split by the spin orbit coupling and the Λ-doubling. Following Tabone et al. (2021), we consider intra- and cross-ladder rotational transitions in the $v = 0$ and $v = 1$ bands as well as between the $v = 1$ and $v = 0$ states, resulting in a total of 2360 (ro-)vibrational transitions.

3. Results

First, we present the results for our fiducial model, which corresponds to a high-pressure ($P_{\mathrm{th}}/k = 10^8$ K cm^{-3}) and strong incident UV field model ($G_0^{\mathrm{incident}} = 10^4$). This model is particularly interesting because these are parameters representative of a PDR for which OH MIR lines are the brightest. We then explore a grid of models to investigate how the line intensities vary with the pressure and incident UV field.
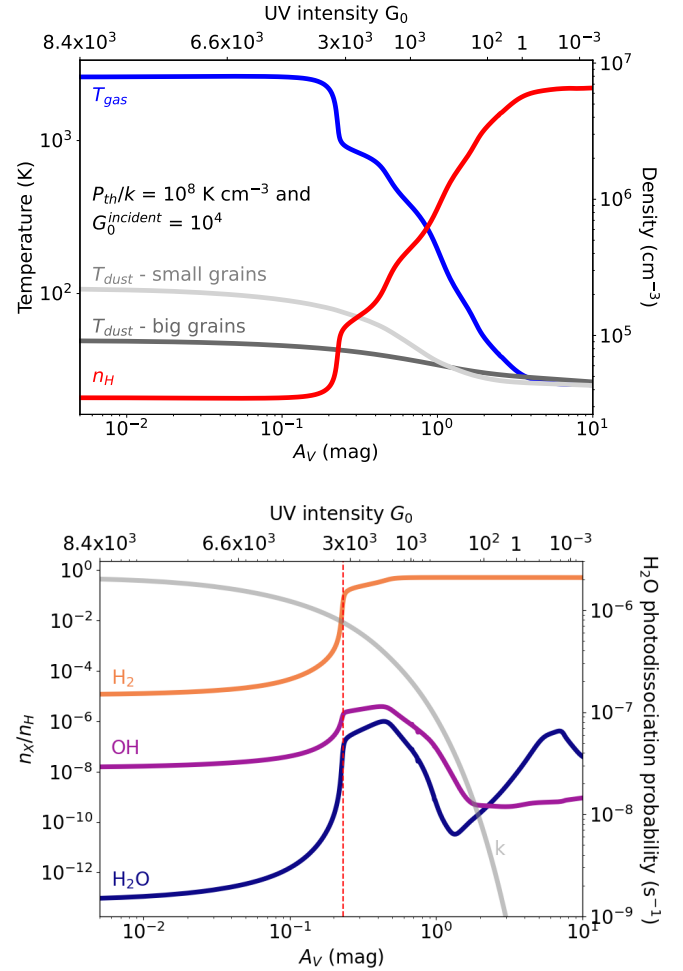
Fig. 1. Results of our fiducial model with $P_{\mathrm{th}}/k = 10^8$ K cm^{-3} and $G_0^{\mathrm{incident}} = 10^4$. (Top panel) Gas density and gas and dust temperature as a function of visual extinction. The size of the small (big) grains is 10^{-7} cm (3.10^{-5} cm). (Bottom panel) H_2O, OH, and H_2 abundances as a function of visual extinction. H_2O photodissociation rate k (s^{-1}) is also represented in light gray. The vertical red line shows the position of the H^0/H_2 transition. The local UV field intensity is given at seven different positions at the top of the graph.

3.1. High-pressure and UV field fiducial model

3.1.1. H_2O density profile and UV field

Figure 1 shows the total hydrogen density and gas temperature (top panel), and the H_2O, OH, and H_2 abundances (bottom panel) across the PDR. The H_2O photodissociation rate is also displayed in the bottom panel. Because thermal pressure is assumed to be constant across the PDR, the gas gets denser as the temperature drops with depth. Until $A_V = 0.1$, the thermal balance is dominated by heating by the photoelectric effect, and [OI] and [CII] radiative cooling. Then, at the H^0/H_2 transition (driven by dust opacity and self-shielding), the temperature decreases steeply as the gas is primarily cooled down by H_2 emission and as the heating by photoelectric effect is less efficient due to the attenuation of the FUV field. Deeper into the PDR ($A_V > 1$), the gas temperature smoothly decreases due to the cooling by CO, and eventually by gas-grain thermal coupling (Tielens & Hollenbach 1985a).

The H_2O and OH abundance profile reflects that of H_2 and of the temperature. Two peaks in H_2O abundance, corresponding to two distinct reservoirs of water are highlighted in
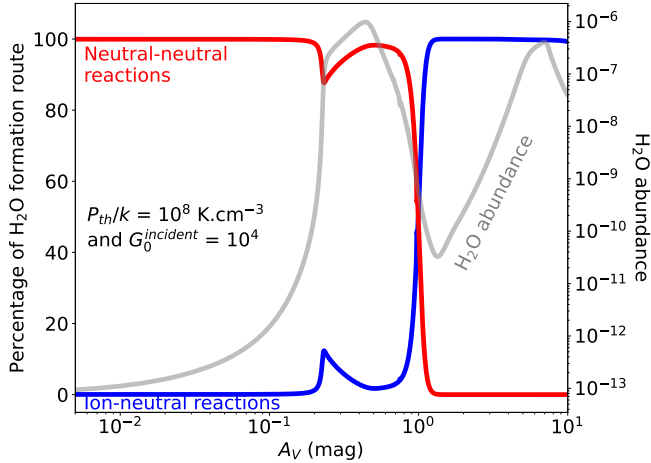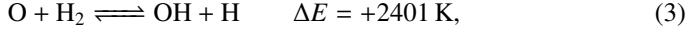
Fig. 2. Percentage of the different formation routes of H_2O as a function of the visual extinction for the model $P_{th}/k = 10^8 \, \mathrm{K \, cm^{-3}}$ and $G_0^{incident} = 10^4$. The blue line represents the percentage of the ion–neutral formation route, and the red line represents the percentage of the neutral–neutral formation route, which requires high temperatures ($T_K \gtrsim 300$ K). The increase in the ion–neutral formation route around $A_V = 0.2$ is due to the increase in OH^+ following neutral–neutral formation of OH. It is therefore associated with warm chemistry.

the bottom panel of Fig. 1. The first peak at $A_V \sim 0.5$ in the warm and irradiated region is mainly due to neutral–neutral reactions (see Fig. 2). Here, H_2O forms primarily via a two-step process with energy barriers (ΔE; van Dishoeck et al. 2013, see Appendix A.1):

$$O + H_2 \rightleftharpoons OH + H \qquad \Delta E = +2401 \text{ K}, \qquad (3)$$
$$OH + H_2 \rightleftharpoons H_2O + H \qquad \Delta E = +1751 \text{ K}. \qquad (4)$$

As the first peak corresponds to an irradiated reservoir of H_2O, OH prompt emission is expected to be confined to that layer. The position of the first H_2O abundance peak is a compromise between being deep enough in the cloud to have relatively abundant molecular H_2 (not photodissociated) necessary for the formation of water and being sufficiently close to the edge to have a temperature high enough to overcome the energy barrier of the chemical reaction. The peak is indeed located close to the H^0/H_2 transition, in agreement with the study of Sternberg & Dalgarno (1995, see their Figs. 8 and 9). Therefore, the peak abundance of H_2O is highly sensitive to the temperature, as further shown in Sect. 3.2 and in Appendix A.2. Interestingly, in the warm region of interest, the inclusion of the enhanced reactivity of excited H_2 in the formation of OH (and therefore H_2O) does not drastically change the results obtained with calculations with the thermal rates. For example, at the H_2O abundance peak, the formation rate of H_2+O is only increased by a factor 2, compared to the formation rate calculated with the thermal rate which is rather low for these orders of magnitude. This is related to the relatively modest endoergicity of reaction $O + H_2$ compared to hydrogenation reactions of N and S^+ (e.g., Goicoechea & Roncero 2022). This lower endoergicity results in relatively high rate coefficients for the lower vibrational H_2 states. In the warm region, OH is also primarily produced by neutral–neutral reactions (see Eq. (3) and Appendix B) with a significant contribution of H_2O photodissociation at the peak of OH abundance. However, as explained in Sect. 3.1.2, only water photodissociation can lead to OH excited in highly rotational states. Thus, OH MIR emission depends on water abundance and not directly on OH abundance.
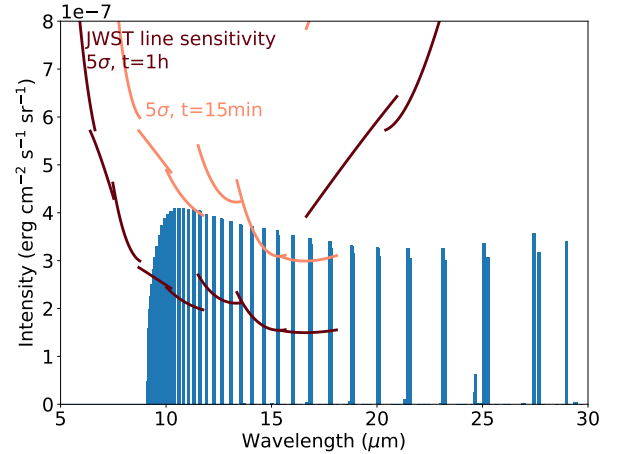

Fig. 3. Intensities of OH MIR lines observed with a viewing angle of $60°$ as a function of wavelength for a model $P_{th}/k = 10^8 \, \mathrm{K \, cm^{-3}}$ and $G_0^{incident} = 10^4$. The brown and orange lines represent the JWST sensitivity for corresponding integration time and an S/N of 5 (Glasse et al. 2015).

Deeper into the PDR ($A_V > 0.5$), the H_2O and OH abundances decrease drastically because the temperature is dropping and both molecules are still efficiently destroyed by photodissociation (see the H_2O photodissociation rate in the bottom panel of Fig. 1). The second water reservoir peaks deeper into the cloud in colder regions, with a peak in H_2O abundance at $A_V \simeq 7$. In this region, H_2O is primarily formed via ion–neutral reactions, ending with the electronic recombination of H_3O^+:

$$OH^+ \xrightarrow{H_2} H_2O^+ \xrightarrow{H_2} H_3O^+ \xrightarrow{e^-} H_2O, \qquad (5)$$
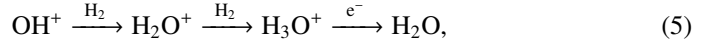
OH^+ being formed by $O + H_3^+$ in molecular regions (see Fig. 2 and Appendix A.2). Water is still primarily destroyed by photodissociation with an efficiency that decreases with depth into the PDR (see light gray in Fig. 1). Thus the H_2O abundance increases again with A_V. We note that deep into the cloud, H_2O formation on grains followed by desorption (not included in our model) is expected to be relevant (Hollenbach et al. 2009; Putaud et al. 2019). However, this cold component is not of interest in the present study because it produces a negligible amount of highly excited OH. Indeed, although the cold reservoir is larger than the warm reservoir, it is so weakly irradiated that the amount of photodissociated water coming from this region is negligible in comparison to that coming from the warm region.

Interestingly, the amount of warm H_2O ($N(H_2O) \sim 4 \times 10^{14} \, \mathrm{cm^{-2}}$) represents only 5–15% of the total H_2O content of the PDR. This is in agreement with the results of Putaud et al. (2019), which suggest that the cold component dominates the emission of H_2O in *Herschel* data. This explains why we cannot use these previous results to predict OH MIR emission, as we are only interested in the warm reservoir.

3.1.2. Prediction of OH MIR lines

Figure 3 presents the calculated MIR spectrum of OH for our fiducial model with a viewing angle of $60°$. The viewing angle is the angle between the line of sight and the normal to the PDR, with $0°$ being face-on and $90°$ edge-on. The value of $60°$ is representative of the inclination of most of the observed interstellar PDRs, as they are closer to being edge-on than face-on (e.g., the Orion Bar and the Horsehead Nebula). A series of pure rotational lines can be seen in the 9–27 μm range coming from high-N
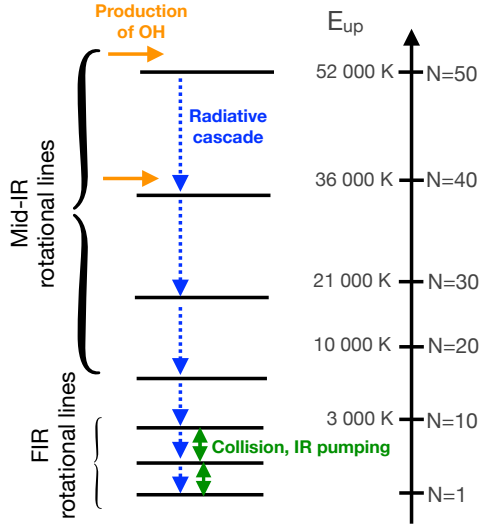
Fig. 4. Schematic of the excitation of OH in the presence of prompt emission. The production of rotationally excited OH (orange arrows) is followed by a $N \rightarrow N-1$ radiative cascade (shown as blue arrows) emitting the series of lines shown in Fig. 3. For lower rotational states ($N \lesssim 10$), OH levels can be excited by IR pumping and collisions that emit in the FIR. In this greatly simplified schematic, only a limited number of rotational levels are shown, ignoring the splitting of rotational levels caused by Λ-doubling and spin-orbit coupling, vibrational levels, and other kinds of weaker radiative transitions.

Fig. 5. Cumulative intensity (normalized) of the 10.8 μm OH line, and of several rotationnal and ro-vibrational lines of H_2 calculated with the Meudon PDR code with a thermal pressure $P_{th}/k = 10^8$ K cm^{-3} and $G_0^{incident} = 10^4$. OH MIR emission traces a thin layer close to the H^0/H_2 transition.

states ($15 \leq N \leq 45$) with upper energies >5000 K. These pure intra-ladder rotational lines, which are split into four components by Λ-doubling and spin–orbit coupling (not apparent in Fig. 3), dominate the MIR OH spectrum. There is a steep increase in line intensity with decreasing N shortward of $\lambda = 10$ μm (N ≃ 35) and then a slow decrease longward of $\lambda = 10$ μm.

Figure 4 summarizes the excitation process leading to the observed prompt emission spectrum shown in Fig. 3. Infrared radiative pumping cannot excite these lines due to the high energy of the upper levels. De-excitation by stimulated emission by the IR background is also negligible because of the small photon occupation number. Collisional excitation cannot populate the upper levels due to their very high upper-energy level, and collisional de-excitation is negligible due to the very high critical densities of these levels ($n_{crit} \geq 10^{13}$ cm^{-3}). Hence, the populations of the levels are only set by the radiative cascade following H_2O photodissociation forming OH in high-N states.

In particular, we recover the result of Tabone et al. (2021), namely that the OH MIR line intensities are only proportional to the column density of water photodissociated in the $\tilde{B}$ band (114 nm < λ < 143 nm):

$$\Phi_B = \int_z F_{pd}(z) dz, \tag{6}$$

where we recall that F_{pd} is the (volumic) destruction rate of H_2O via photodissociation in the 114–143 nm UV range (see Eq. (2)). This simple result demonstrates that OH MIR lines give direct access to H_2O photodissociation but no (direct) information on the column density of OH, the density, or the temperature. H_2O abundance in irradiated media being highly sensitive to the physical conditions (in particular temperature), OH MIR lines are in turn an indirect but very sensitive diagnostics of the physical conditions.
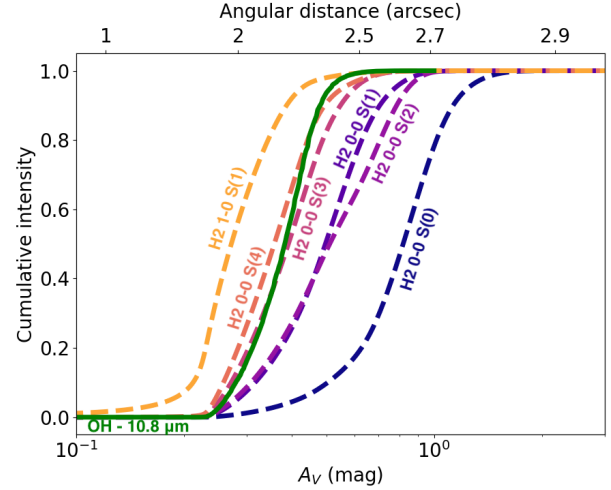
We also recover that the overall shape of the MIR spectrum of OH neither depends on OH column density nor on the photodissociated column density of H_2O Φ_B. Indeed, as discussed in Tabone et al. (2021), the relative intensity of the excited lines is only set by the distribution of nascent OH, which is set by the spectral shape of the UV field. However, in this work, we neglect the effect of the shape of the radiation field within the 114–143 nm range and we take the distribution of OH at Ly-α wavelength (121 nm) as a representative wavelength. Therefore, the intensity of each line shown here is, by construction, only proportional to Φ_B and does not depend on other parameters. In the following, we focus our study on the total intensity of the $N = 30 \rightarrow 29$ quadruplet at 10.8 μm as it is the brightest of the spectrum.

In order to locate the emitting region of rotationally excited OH emission in the PDR, we calculate the cumulative intensity[2] as a function of the PDR depth. Figure 5 compares the cumulative intensity of the 10.8 μm OH line and rotationally excited H_2 lines across the PDR. First, this figure shows that OH emission is confined to a thin layer around $A_V \simeq 0.4$ that corresponds to the H^0/H_2 transition. It can also be seen that this OH line peaks at the same position as the relatively excited H_2 pure rotational lines such as 0–0 S(3) and 0–0 S(4). H_2 rotational lines are excited by collision and so their emitting region reflects the temperature gradients across the PDRs. Thus, 0–0 S(3) ($E_u/k \sim 2504$ K) and 0–0 S(4) ($E_u/k \sim 3474$ K) peak closer to the edge than less excited lines such as 0–0 S(0) ($E_u/k \sim 510$ K), which has a lower upper energy level. The H_2 1–0 S(1) line ($E_u/k \sim 6952$ K) is mainly populated by UV pumping. This explains why this line emission peaks closer to the edge at the H^0/H_2 transition.

We note that H_2 rotational lines are a good diagnostic of the gas temperature as they are close to local thermodynamical equilibrium and are optically thin. However, this diagnostic needs high angular resolution to separate the emitting region of each lines; otherwise, the line fluxes are averaged on the PDR. The gas temperature profile can therefore only be measured with the H_2 lines in close and sufficiently wide PDRs. In the cases where the observations are not spatially resolved, OH MIR lines can be a unique indirect diagnostic with which to probe temperature at

---

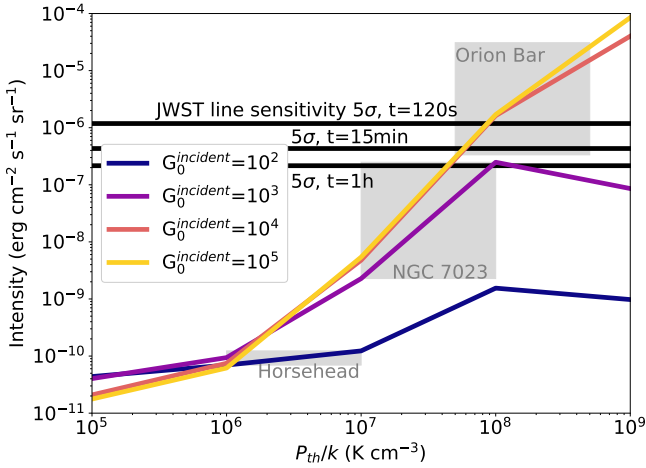[2] $I(A_V)/I(A_V = 20)$ assuming OH and H_2 lines are optically thin.

Fig. 6. Summed intensity of the quadruplet at $\lambda = 10.8\,\mu m$ observed with a viewing angle of $60°$ as a function of the gas pressure for different UV field intensities. The black horizontal lines represent the JWST sensitivity for a corresponding integration time and an S/N of 5.

the H^0/H_2 transition as OH MIR emission is strongly correlated to the thermal balance due to the need for high temperatures for the formation of H_2O.

3.2. Effects of thermal pressure and UV field

As shown in Sect. 3.1.2, OH MIR emission is directly proportional to the amount of photodissociated water, water abundance being very sensitive to the temperature and the local UV field. Therefore, one would naturally expect a strong dependency of the OH line intensity on the thermal pressure and the strength of the incident UV radiation field. In this section, we study a grid of models with pressure ranging from $P_{th}/k = 10^5$ to $10^9\,K\,cm^{-3}$ and incident UV field intensity in the range of $G_0^{incident} = 10^2$ to 10^5.

Figure 6 summarizes the evolution of the $10.8\,\mu m$ line intensity as a function of the thermal pressure for different UV field intensities. It can be seen that OH emission depends strongly on the thermal pressure (see Sect. 3.2.1 for further explanation). On the other hand, for UV field intensity $G_0^{incident} > 10^3$, OH line intensities do not depend significantly on incident UV field intensity (see Sect. 3.2.2 for further explanation). To understand this result, we study the evolution of the temperature and UV field intensity at the warm peak of H_2O as a function of the thermal pressure and the intensity of the UV field $G_0^{incident}$ as presented in Fig. 7.

3.2.1. Dependence on pressure

Figure 7a displays the abundance profile of H_2O for different thermal pressures. It shows that we still recover a peak in H_2O abundance down to $P_{th}/k = 10^6\,K\,cm^{-3}$, corresponding to the warm and irradiated reservoir of H_2O that produces rotationally excited OH. As thermal pressure increases, the warm H_2O reservoir moves closer to the edge and the corresponding peak abundance of H_2O increases dramatically by six orders of magnitude from $P_{th}/k = 10^6$ to $10^9\,K\,cm^{-3}$. This result might be surprising because at high pressure, the warm reservoir is more irradiated (see Fig. 7c, blue curve) and therefore H_2O is more efficiently photodissociated. The density also increases with pressure, which directly enhances the formation rate of H_2O in proportion. However, this effect is not enough to account

for the dramatic increase in H_2O abundance. In fact, as pressure increases, the gas at the H^0/H_2 transition gets warmer (see Fig. 7c, red curve), triggering active OH and H_2O formation via neutral–neutral reactions. Therefore, the steep increase in H_2O abundance with P_{th}/k is primarily due to the gas temperature rising. We still notice that the temperature increase is an indirect consequence of the increase in density and local UV field at the H^0/H_2 transition, because the H_2 forms closer to the PDR edge at high densities, and heating by H_2 UV pumping and H_2 formation are enhanced.

The sensitivity of the formation route of H_2O on temperature is further highlighted in Fig. 8, where the calculated abundance of H_2O is compared to our analytic model of oxygen chemistry detailed in Appendix A. We recover the fact that down to $P_{th}/k \simeq 10^7\,K\,cm^{-3}$, H_2O is primarily formed by neutral–neutral reactions, and that the efficiency of this route declines for lower thermal pressures due to lower temperatures. Interestingly, at very low pressure, below $P_{th}/k \simeq 10^6\,K\,cm^{-3}$, the ion–neutral reaction, which is weakly dependent on temperature, takes over from the neutral–neutral route. This roughly corresponds to the thermal pressure below which the peak in warm H_2O abundance disappears.

We recall that MIR OH line intensities are proportional to the quantity of H_2O that is photodissociated, which is the product of the H_2O density profile and the UV field flux integrated over the cloud. This explains why OH MIR lines are found to increase with thermal pressure (see Fig. 6): H_2O is more efficiently formed via neutral–neutral reactions in the warm molecular layer and, to a lesser extent, because that reservoir is more irradiated (see Figs. 7 and 8).

3.2.2. Dependence on incident UV field

Figure 7b displays the H_2O abundance profile for different strengths of incident UV field and $P/k = 10^8\,K\,cm^{-3}$. As the strength of the incident UV field increases, the warm H_2O reservoir moves deeper into the cloud. The H^0/H_2 transition is indeed shifted to larger A_V because the total column density needs to be higher to trigger the H^0/H_2 transition. The H_2O peak abundance is also somewhat reduced for stronger incident UV fields. This is due to both a slight decline in temperature, which quenches H_2O formation by the neutral route, and an increase in the local radiation field at the H^0/H_2 transition (see Fig. 7d).

Based on these results, we come to the conclusion that MIR OH line intensities, which are proportional to the amount of photodissociated water, depend weakly on the incident UV field intensity for $G_0^{incident} \gtrsim 10^3$. Indeed, as the incident UV field increases, the amount of H_2O decreases slowly but the local radiation field increases accordingly. Both effects tend to act against each other for OH MIR emission, resulting in a weaker dependency on the incident UV field than on thermal pressure, at least for $G_0^{incident} > 10^3$, where the H_2O abundance seems to saturate with increasing incident UV field.

3.2.3. Evolution of the OH/H_2 line ratio

The predicted line intensities depend on the inclination of the PDR which is a major source of uncertainty in observations. Therefore, we present a more robust prediction in Fig. 9, namely the ratio between the $10.8\,\mu m$ OH line and the $2.12\,\mu m$ H_2 rovibrational line, which peaks at a position close to that of OH and has already been observed at high angular resolution (e.g., Habart et al. 2022).
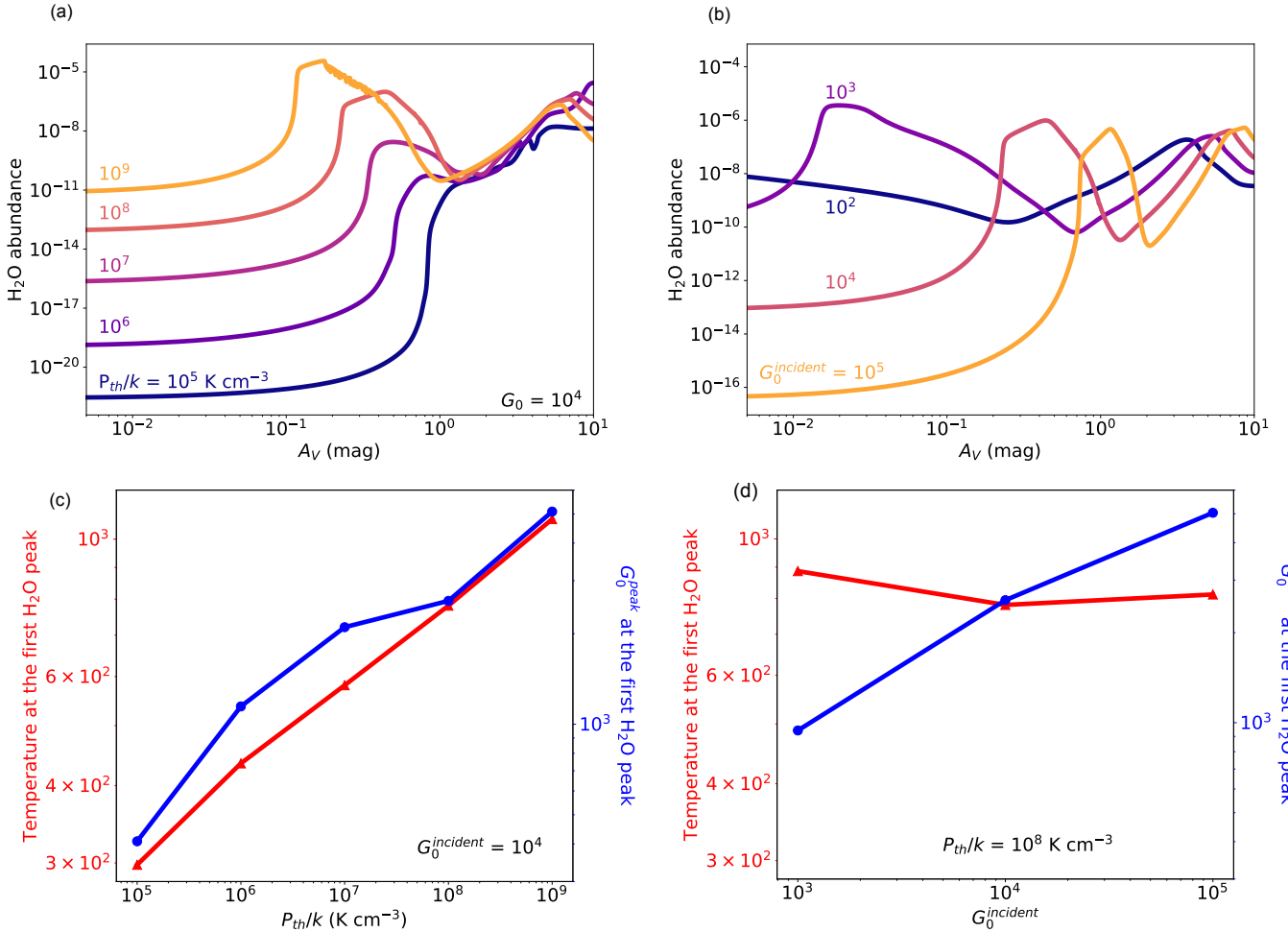
Fig. 7. Evolution of H_2O abundance, local gas temperature, and local UV field as a function of the thermal pressure and the incident UV field. Top panels: Abundance profile of H_2O for different thermal pressures at a given UV field intensity (a) and for different incident UV fields at a given thermal pressure (b). Bottom panels: Evolution of the temperature and the UV field at the first H_2O peak as a function of the thermal pressure (c) and the incident UV field intensity (d).

Figure 9 shows that the ratio is not constant and that over $P_{th}/k \geq 10^6 \, \mathrm{K \, cm^{-3}}$, the ratio increases. The higher the pressure is, the higher the warm gas quantity. This fosters warm H_2O formation by neutral–neutral reactions and thus fosters the formation of OH, which emits in the MIR. The H_2 1–0 S(1) line increases with pressure as it is proportional to the gas density (for $n_H/G_0 < 40 \, \mathrm{cm^{-3}}$ e.g., Burton et al. 1990) but it is not dependent on the gas temperature.

4. Application to the Orion Bar and other environments

4.1. Orion Bar

The Early Release Science program "PDRs4All: radiative feedback from massive stars" (Berné et al. 2022) for the JWST observations is dedicated to studying the interactions of massive stars with their surroundings. The target of this program is a well-known PDR: the Orion Bar. This region will be observed through NIRSpec, NIRCam, and MIRI, providing IFU spectroscopy with NIRSpec and MIRI, and imaging with NIRCam and MIRI. In this section, we use predictions for the Orion Bar to illustrate the potential of OH and discuss the main limitations of upcoming JWST observations of interstellar PDRs.

4.1.1. Predicted OH line intensities

The parameters used in the models of the Orion Bar are summarized in Table 2. We consider an isobaric model with a pressure ranging from $P_{th}/k = 5 \times 10^7 \, \mathrm{K \, cm^{-3}}$ to $P_{th}/k = 5 \times 10^8 \, \mathrm{K \, cm^{-3}}$, in agreement with previous studies (Allers et al. 2005; Joblin et al. 2018). We adopt an incident UV field coming from an illuminating O7 star with an effective temperature $T_{\mathrm{eff}} = 40\,000 \, \mathrm{K}$ modeled by a blackbody at T_{eff}.

The UV field intensity is taken equal to 2.10^4 in Mathis units which is in agreement with previous estimates giving $G_0^{\mathrm{incident}} = 1 - 4 \times 10^4$ (Tielens & Hollenbach 1985b; Marconi et al. 1998). We assume the extinction curve HD 38087 of Fitzpatrick & Massa (1990) and $R_V = 5.62$, which is close to the value determined for the Orion Bar of 5.5 (Marconi et al. 1998). This extinction curve is also in agreement with the recent dust study by Schirmer et al. (2022) who worked with the THEMIS dust model in the Orion Bar with nano-grain depletion.

These models include an exact radiative-transfer calculation for the UV pumping of H_2 lines originating from the first 30 levels of H_2, while the other lines are treated using the FGK approximation (Federman et al. 1979). This allows mutual shielding effects between overlapping H_2 and H UV absorption lines to be accounted for. This approximation can affect the position of the H^0/H_2 transition as the FGK approximation tends to
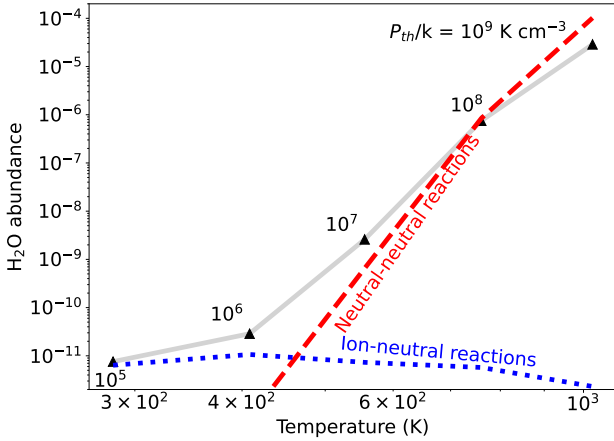
Fig. 8. Analytic calculations of the first H$_2$O peak abundance as a function of the temperature at the first H$_2$O peak (Appendix A, using the thermal rate coefficient from Agúndez et al. 2010; Veselinova et al. 2021). The state-specific rate coefficients are not considered in the analytic calculations. Using the state-specific chemistry enhances the abundance of H$_2$O by a factor 2. The dotted blue line represents the calculation of the abundance of H$_2$O formed by ion–neutral reactions and the dashed red line represents the calculation of the abundance of H$_2$O formed by neutral–neutral reactions. The triangles are the first H$_2$O peak abundances calculated with the Meudon PDR code for models at incident UV field $G_0^{incident} = 10^4$ and different thermal pressure.

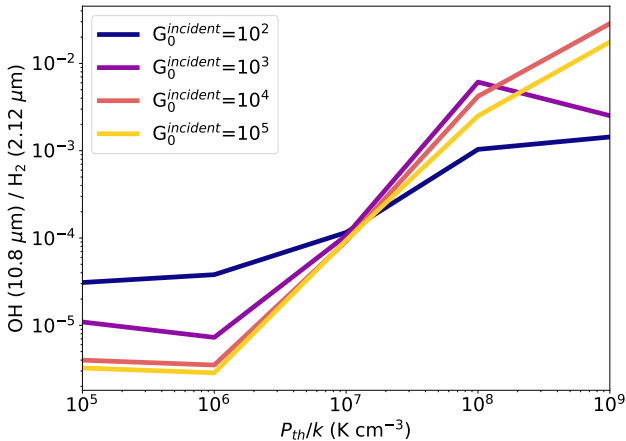**Fig. 9.** Ratio of the predicted OH line at 10.8 μm over the H$_2$ line 1–0 S(1) at 2.12 μm predicted by the Meudon PDR Code.

shift the H^0/H$_2$ transition closer to the edge of the cloud, slightly affecting the abundance of H$_2$O in the warm layer. However, the emerging line intensities of OH and H$_2$ are little affected (less than 10%).

To estimate the absolute intensity of the OH MIR lines, we consider the ratio of the OH lines to the H$_2$ 1–0 S(1) line at 2.12 μm predicted by the model multiplied by the H$_2$ 1–0 S(1) line intensity recently measured by the *Keck* Telescope (Habart et al. 2022) at an angular resolution (0.1″) similar to that of the JWST. Indeed, OH and H$_2$ lines originate from roughly the same region in the PDR (see Fig. 5) and so the intensity of these lines will be affected in the same way by geometry effects. Through the position of the JWST/NIRSpec–IFU and MIRI–IFU mosaics of the ERS program, the 1–0 S(1) line was measured at an intensity of 8.7×10^{-4} erg cm^{-2} s^{-1} sr^{-1} at the dissociation front.

The H$_2$ line intensity at 2.12 μm needs to be corrected for extinction due to the foreground dust and internal dust in the

Table 2. Input parameters of the Meudon PDR code for the Orion Bar model.

Parameters	Values
A_V^{tot}	10
P_{th}/k (K cm^{-3})	5×10^7–5×10^8
G_0^{incident} (Mathis unit)	2×10^4
UV field shape	Blackbody at 40 000 K
Transfer	Full line
Cosmic rays (s^{-1} per H$_2$)	5×10^{-17}
R_V	5.62
N_{H}/E(B-V) (cm^{-2})	1.05×10^{22}
Dust to gas ratio	0.01
Grain size distribution	$\propto \alpha^{-3.5}$
Min grain radius (cm)	1×10^{-7}
Max grain radius (cm)	3×10^{-5}

Bar itself. As discussed in Habart et al. (2022), the H$_2$ line is expected to be about 56% brighter in total (16% for the foreground dust and 40% for the internal dust). This is in agreement with the total extinction correction derived by Kaplan et al. (2021). This leads to an extinction-corrected intensity of 1.4×10^{-3} erg cm^{-2} s^{-1} sr^{-1}. OH lines at longer wavelengths are mostly not affected by dust extinction. It is only at shorter wavelengths that dust extinction will significantly attenuate the emission. The different OH/H$_2$ line ratios and the estimated OH line intensity are presented in Table 3.

The line sensitivity of MIRI MRS (medium-resolution spectroscopy) is about 1×10^{-6} erg cm^{-2} s^{-1} sr^{-1} for a S/N of 5 and an integration time of 111 s, which is granted for the ERS program. The intensities for lines around 10 μm are about 1×10^{-6} erg cm^{-2} s^{-1} sr^{-1} for the lower limit model at $P_{\text{th}}/k = 5 \times 10^7$ K cm^{-3} and around 1×10^{-5} erg cm^{-2} s^{-1} sr^{-1} for the upper limit model at $P_{\text{th}}/k = 5 \times 10^8$ K cm^{-3} (see Table 3). Both lines might be detected for the upper limit model only considering the estimated intensities. However, it is also possible to stack different lines to increase the S/N and detect them even in the lower limit model. Nevertheless, the main limitation for detection of OH MIR lines in PDR is the small contrast between the strong continuum and the weak OH lines, as explained in the following section.

4.1.2. Predicted spectrum with continuum and other lines

To study the detectability of OH lines, we estimated the continuum and the other gas lines at the H^0/H$_2$ dissociation front where the OH line emission peaks. OH lines could blend with other lines but most importantly could be lost in the continuum noise due to instrumental defaults such as fringing. It is therefore necessary to have OH lines over the continuum greater than the noise expected on the continuum (predicted to be of the order of 1%). To estimate the dust continuum and other lines, we used the synthetic spectro-imaging cube from the ERS program. This cube was computed using the maps of five regions of the PDR and five template spectra of these regions[3]. The template spectra were determined using the PDR code for atomic and molecular line contributions (Le Petit et al. 2006); CLOUDY for the ionized gas (Ferland et al. 1998); the model PAHTAT for PAH emission

---

[3] The Orion Bar synthetic spectra are available here https://pdrs4all.org/seps/#Orion-Bar-synthetic-spectra

Table 3. OH/H$_2$(2.12 μm) line ratio and estimated OH line sum intensity of the quadruplet for different models.

Models	$P_{th}/k = 5 \times 10^7$ K cm^{-3}	$P_{th}/k = 5 \times 10^8$ K cm^{-3}
OH(9.9 μm)/H$_2$(2.12 μm)	7.6×10^{-4}	8.7×10^{-3}
OH(10.8 μm)/H$_2$(2.12 μm)	8.1×10^{-4}	9.2×10^{-3}
9.9 μm OH line intensity (erg cm^{-2} s^{-1} sr^{-1})	1.0×10^{-6}	1.2×10^{-5}
10.8 μm OH line intensity (erg cm^{-2} s^{-1} sr^{-1})	1.1×10^{-6}	1.3×10^{-5}
Integration time	Sensitivity at 9.9 μm (erg cm^{-2} s^{-1} sr^{-1}) - S/N = 5	Sensitivity at 10.8 μm
111 s	1.4×10^{-6}	1.2×10^{-6}
15 min	5.0×10^{-7}	4.3×10^{-7}

Notes. Sensitivity of the JWST for a S/R of 5.
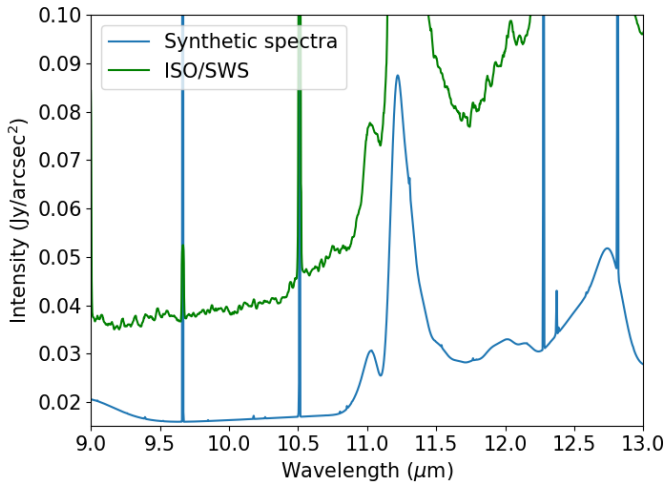
Fig. 10. Synthetic spectrum at the H^0/H$_2$ dissociation front from the synthetic cube made for the future MIRI observation in the ERS program (Berné et al. 2022) ($R \sim 3000$) and *ISO*-SWS spectrum ($R \sim 1500$).

(Pilleri et al. 2012) using the template spectra extracted by Foschino et al. (2019) on *ISO*-SWS data using machine learning algorithms; and finally the THEMIS dust model (Jones et al. 2013, 2017) with the radiative transfer code SOC (Juvela 2019) for the dust continuum emission following the approach of Schirmer et al. (2022). This dust model is based on *Spitzer* and *Herschel* observations in five photometric bands (3.6, 4.5, 5.8, 8, and 70 μm). Observations at 24 μm of the Orion Bar exist but are saturated. We compare the model to available observations, namely *ISO*/SWS observations centered on the PDR with a large beam (20") and *Spitzer*-IRAC maps. *Spitzer*-IRS spectra are only available in the atomic region at the peak of the MIR dust continuum. The model accurately reproduces the *Spitzer*-IRAC observations at 3.6 and 8 μm. However, longward of 8 μm, the continuum in the synthetic spectrum is three times weaker than that measured in the *ISO*-SWS spectrum (see Fig. 10). Nevertheless, the *ISO*-SWS spectrum does not spatially resolve the PDR and mixes the peak of the continuum observed in the atomic zone with *Spitzer*/IRAC and the peak of the lines of H$_2$ and OH expected at the dissociation front. JWST will spatially resolve the different PDR layers, allowing us to properly verify the model and determine if the continuum is actually underestimated for $\lambda > 8$ μm.

Figure 10 displays the spectrum at the H^0/H$_2$ dissociation front derived from the synthetic cube. We focus here on the wavelength range 9–13 μm because as seen in Fig. 3 this is the domain where OH lines are the brightest. Moreover, longward of 15 μm, OH lines might also be excited by other mechanisms such as chemical pumping by O+H$_2$ with ro-vibrationally excited H$_2$ (A. Zanchet, priv. comm., and preliminary results from Maiti & Schatz 2003; Braunstein et al. 2004; Weck et al. 2006) or with the first excited state of oxygen O(^{1}D) (Liu et al. 2000) and not only from water photodissociation.

4.1.3. Line-continuum ratio

Figure 11 shows the OH line-to-continuum ratio for models with different thermal pressure. In order to compute this latter, OH line spectra were calculated by considering the integrated intensities divided by the frequency width equal to the spectral resolution element. The spectra were then divided by the simulated spectrum including the continuum and other gas lines as described in the previous subsection. The ratio is much higher for the $P_{th}/k = 5 \times 10^8$ K cm^{-3} model than for the $P_{th}/k = 5 \times 10^7$ K cm^{-3} model, as expected from the analysis of Sect. 3.2.1. The line-to-continuum variation results from the OH line intensity distribution as seen in Fig. 3 and the shape of the dust emission continuum, aromatic bands, and bright lines in this region as seen in Fig. 10. The overall shape is similar for both models because, as explained in Sect. 3.1.2, the relative intensities of the intra-ladder lines depend only on the spectral shape of the UV field, which here is the same for both models. The ratio of OH lines over the continuum is maximum around 10 μm. This is a result of a combined effect between OH line intensities reaching their maximum around 10.8 μm and continuum increasing progressively after 10 μm. The lines around 10 μm are therefore those with the highest probability of being detected with the JWST. The value of the maximum ratio varies from 0.6% for a lower limit model at $P_{th}/k = 5 \times 10^7$ K cm^{-3} to 7% for an upper limit model at $P_{th}/k = 5 \times 10^8$ K cm^{-3}. The continuum could be underestimated after 8 μm, which can lead to smaller ratios. Therefore, the detection should be possible for the upper limit model at $P_{th}/k = 5 \times 10^8$ K cm^{-3}, while it will be more challenging for the lower limit model at $P_{th}/k = 5 \times 10^7$ K cm^{-3}.

4.1.4. Possible blending with other lines

There are also intense lines such as H$_2$ rotational lines (0–0 S(2) and 0–0 S(3)), aromatic bands or lines from the ionized gas (NeII at 12.8 μm, SIV at 10.5 μm, etc.), which could blend with OH lines. Figure 12 displays a zoom onto the 10 μm zone of the spectrum where OH lines are added with a resolving power of 3000. This specific wavelength domain was chosen because
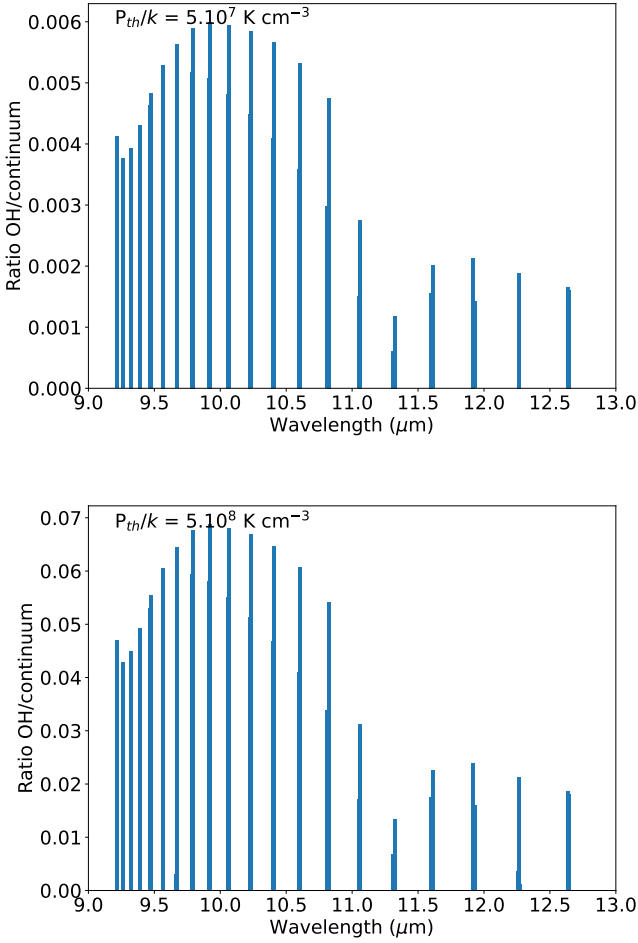
Fig. 11. Ratio of OH lines over the continuum. Top panel: $P_{th}/k = 5.10^7\,\mathrm{K\,cm^{-3}}$ and $G_0^{\mathrm{incident}} = 10^4$. Bottom panel: $P_{th}/k = 5.10^8\,\mathrm{K\,cm^{-3}}$ and $G_0^{\mathrm{incident}} = 10^4$. The main difference from the variation of the OH line intensities seen in Fig. 3 is at 11.3 μm where the ratio drops drastically due to the aromatic band (at 11.3 μm).

this is where the line over continuum ratio is the highest (see Fig. 11). On this figure, the line seen at 9.67 μm is the H₂ 0–0 S(3) line. This figure highlights the fact that OH lines are drastically less intense than other lines. Moreover, the 9.9 μm quadruplet is only partially resolved with a resolving power of 3000 (close to the JWST resolving power at this wavelength). Indeed, only two peaks are visible instead of the four expected (at 9.914 μm, 9.916 μm, 9.923 μm and 9.924 μm). However, this figure shows that in the region where the line-to-continuum ratio is the highest, no other lines should blend with OH lines.

In summary, this study shows that in terms of intensity, it is probable that OH lines are detectable as long as the thermal pressure is not too low. The main difficulty in detecting those lines lies in the line-to-continuum ratio. Indeed, as seen in Sect. 4.1.3, even in the best case scenario, the line-to-continuum ratio will not exceed 1%-7%. The possible detectability of OH lines relies on the low level of noise. The noise has to be below the line-to-continuum ratio to enable detection.

4.2. Application to other environments

4.2.1. Other interstellar PDRs

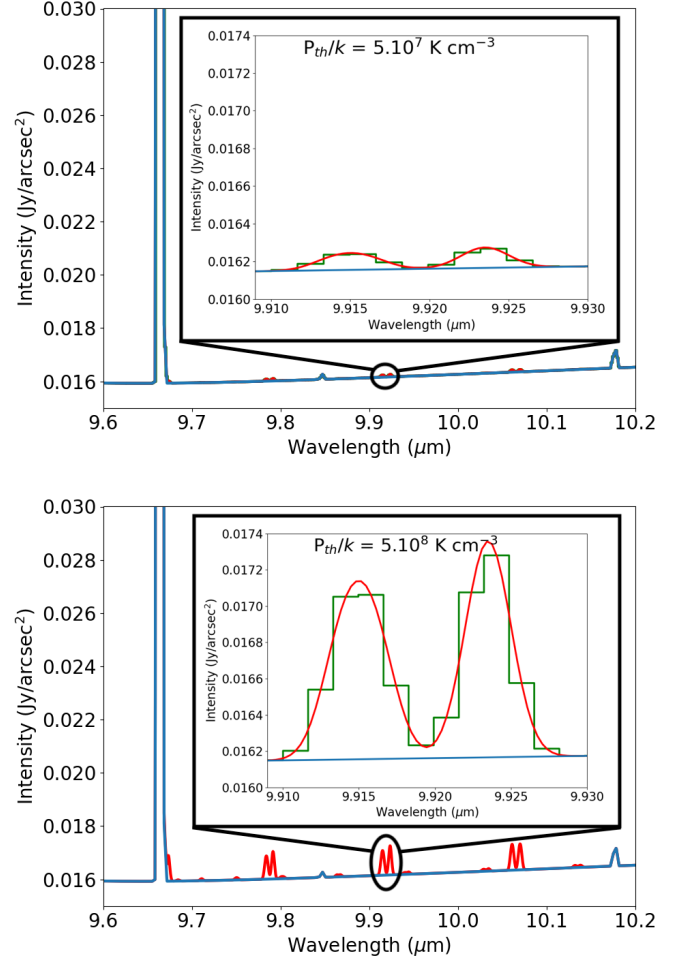Figure 6 and Sect. 3.2 show that OH MIR lines can only be detected in very illuminated PDRs with high pressure due to

Fig. 12. Spectrum near the dissociation front at the position chosen for the MIRI IFU observation with the ERS (Berné et al. 2022) around 10 μm (blue) with the addition of OH lines (red) for a spectral resolving power $R = 3000$. The line at 9.67 μm is the H₂ 0–0 S(3). The sampling, represented with the green line, is half the element of resolution around 10 μm (as Fig. 7 from Glasse et al. 2015); it is about 1.7×10^{-3} μm near 10 μm for $R = 3000$. (Top panel) $P_{th}/k = 5.10^7\,\mathrm{K\,cm^{-3}}$ and $G_0^{\mathrm{incident}} = 10^4$. (Bottom panel) $P_{th}/k = 5.10^8\,\mathrm{K\,cm^{-3}}$ and $G_0^{\mathrm{incident}} = 10^4$. The 9.9 μm quadruplet is only partially resolved with a resolving power of 3000. Only two peaks are visible instead of the four expected (at 9.914 μm, 9.916 μm, 9.923 μm and 9.924 μm).

the presence of high temperature. In particular, OH MIR lines are expected to be too weak in regions such as the Horsehead nebula because the thermal pressure, and therefore the gas temperature, is too low. Regions such as NGC 7023 might produce sufficiently bright OH lines but these would be at the limit of detection (about $1\times10^{-6}\,\mathrm{erg\,cm^{-2}\,s^{-1}\,sr^{-1}}$ for an integration time of 144 s at a S/N of 5, which is granted for the GTO 1192). What is highlighted in this figure is that very high pressure $P_{th}/k \gtrsim 5.10^7\,\mathrm{K\,cm^{-3}}$ and UV field intensity $G_0 > 10^3$ are necessary to produce supposedly detectable OH MIR lines. Due to this result, the Orion Bar is the best candidate to observe them.

4.2.2. Proplyds

PDRs at the edge of dense molecular clouds are not the only objects where OH lines might be detected by JWST. Our thermochemical modeling shows that, as a rule of thumb, denser irradiated environments (high thermal pressure) result in stronger MIR

OH line fluxes. This result is in line with the previous detections of bright OH lines with *Spitzer*-IRS in several protoplanetary disks (Najita et al. 2010; Carr & Najita 2014, Tabone et al., in prep.) and strong protostellar shocks (Tappe et al. 2008, 2012). JWST programs dedicated to interstellar PDRs will encompass proplyds in their field of view (e.g., ERS PDRs4All, Berné et al. 2022). Because they correspond to very dense clumps of gas ($n_H > 10^8\,cm^{-3}$ Champion et al. 2017), and based on the previous detection of nonexternally irradiated disks, OH MIR lines are expected to be well detected with JWST. In these objects, OH MIR emission will still be directly related to the amount of H_2O photodissociated per unit of time. However, detailed interpretation of the line flux requires dedicated modeling of proplyds, which is beyond the scope of the present paper.

5. Conclusion

In this work, we explored the potential of OH MIR lines for use in the study of interstellar PDRs. In order to achieve this goal, we amended the Meudon PDR code to include prompt emission induced by H_2O photodissociation in the 114–143 nm UV band and a new state-specific formation rate of OH, and analyzed a grid of models.

The main conclusions of this study can be summarized as follows:

1. OH MIR emission is confined to a thin exposed layer close to the H^0/H_2 transition where H_2O is formed by neutral–neutral reactions and is actively photodissociated;

2. OH MIR lines are directly proportional to the column density of water photodissociated in the 114–143 nm range. As water requires high temperature to form, OH MIR lines are very sensitive to the temperature at the H^0/H_2 transition. In particular, we predict that OH MIR lines are brighter in regions with high thermal pressure;

3. OH MIR lines are less dependent on the strength of the incident UV field for $G_0^{incident} > 10^3$. When the incident UV field increases, the H^0/H_2 transition shifts deeper into the cloud but the temperature and local UV field (and thus water abundance) stay rather constant, explaining the rather small impact on OH lines;

4. OH lines are predicted to be detectable with JWST only in highly illuminated PDRs ($G_0^{incident} > 10^3$) with high pressure ($P_{th}/k > 5 \times 10^7\,K\,cm^{-3}$). Detection might then be possible in the Orion Bar but not in the Horsehead Nebula. The low line-to-continuum ratio might also be a major limitation for the detection of OH lines because of instrumental effects such as fringes.

In conclusion, our work demonstrates that OH MIR lines are a promising tool for studying the physical processes in PDRs. In particular, OH MIR lines constitute an indirect but sensitive diagnostic of the temperature at the H^0/H_2 transition, a parameter that is highly uncertain in PDR models (Röllig et al. 2007). Spatially resolved observations of MIR OH and H_2 rotational lines will therefore be key to testing PDR models, better calibrating the correlation between OH emission and temperature, and studying the details of oxygen chemistry in irradiated environments. For nonspatially resolved observations of PDRs, where H_2 emission gives only an average estimate of the temperature, OH would then be a unique diagnostic to assess the temperature around the H^0/H_2 transition. We also note that in this

study, we focused only on the prompt emission of OH induced by H_2O photodissociation at short wavelengths. Prompt emission induced by water photodissociation longward of 143 nm, which excites ro-vibrational lines in the NIR, as well as chemical pumping by O+H_2, which excites MIR lines longward of $\simeq 15\,\mu m$, if properly modeled, can also bring strong complementary constraints on the physical and chemical processes in dense PDRs.

References

Agúndez, M., Goicoechea, J. R., Cernicharo, J., Faure, A., & Roueff, E. 2010, ApJ, 713, 662
Allers, K. N., Jaffe, D. T., Lacy, J. H., Draine, B. T., & Richter, M. J. 2005, ApJ, 630, 368
Bernard-Salas, J., & Tielens, A. G. G. M. 2005, A&A, 431, 523
Bernard-Salas, J., Peeters, E., Sloan, G. C., et al. 2009, ApJ, 699, 1541
Berné, O., Habart, É., Peeters, E., et al. 2022, PASP, 134, 054301
Black, J. H., & van Dishoeck, E. F. 1987, ApJ, 322, 412
Braunstein, M., Adler-Golden, S., Maiti, B., & Schatz, G. C. 2004, J. Chem. Phys., 120, 4316
Brooke, J. S. A., Bernath, P. F., Western, C. M., et al. 2016, J. Quant. Spec. Radiat. Transf., 168, 142
Burton, M. G., Hollenbach, D. J., & Tielens, A. G. G. M. 1990, ApJ, 365, 620
Carr, J. S., & Najita, J. R. 2014, ApJ, 788, 66
Champion, J., Berné, O., Vicente, S., et al. 2017, A&A, 604, A69
Choi, Y., van der Tak, F. F. S., Bergin, E. A., & Plume, R. 2014, A&A, 572, A10
Compiègne, M., Verstraete, L., Jones, A., et al. 2011, A&A, 525, A103
Cox, N. L. J., Pilleri, P., Berné, O., Cernicharo, J., & Joblin, C. 2016, MNRAS, 456, L89
Federman, S. R., Glassgold, A. E., & Kwan, J. 1979, ApJ, 227, 466
Ferland, G. J., Korista, K. T., Verner, D. A., et al. 1998, PASP, 110, 761
Fitzpatrick, E. L., & Massa, D. 1988, ApJ, 328, 734
Fitzpatrick, E. L., & Massa, D. 1990, ApJS, 72, 163
Flower, D. R., & Roueff, E. 1998, J. Phys. B At. Mol. Phys., 31, 2935
Flower, D. R., & Roueff, E. 1999, J. Phys. B At. Mol. Phys., 32, 3399
Foschino, S., Berné, O., & Joblin, C. 2019, A&A, 632, A84
Glasse, A., Rieke, G. H., Bauwens, E., et al. 2015, PASP, 127, 686
Goicoechea, J. R., & Roncero, O. 2022, A&A, 664, A190
Goicoechea, J. R., Joblin, C., Contursi, A., et al. 2011, A&A, 530, L16
Goicoechea, J. R., Pety, J., Cuadrado, S., et al. 2016, Nature, 537, 207
Gonzalez Garcia, M., Le Bourlot, J., Le Petit, F., & Roueff, E. 2008, A&A, 485, 127
Habart, E., Walmsley, M., Verstraete, L., et al. 2005, Space Sci. Rev., 119, 71
Habart, E., Abergel, A., Boulanger, F., et al. 2011, A&A, 527, A122
Habart, E., Le Gal, R., Alvarez, C., et al. 2022, arXiv e-prints, [arXiv:2206.08245]
Heays, A. N., Bosman, A. D., & van Dishoeck, E. F. 2017, A&A, 602, A105
Hogerheijde, M. R., de Geus, E. J., Spaans, M., van Langevelde, H. J., & van Dishoeck, E. F. 1995, ApJ, 441, L93
Hollenbach, D., & Natta, A. 1995, ApJ, 455, 133
Hollenbach, D. J., & Tielens, A. G. G. M. 1999, Rev. Mod. Phys., 71, 173
Hollenbach, D., Kaufman, M. J., Bergin, E. A., & Melnick, G. J. 2009, ApJ, 690, 1497
Inoguchi, M., Hosokawa, T., Mineshige, S., & Kim, J.-G. 2020, MNRAS, 497, 5061
Joblin, C., Bron, E., Pinto, C., et al. 2018, A&A, 615, A129
Jones, A. P., Fanciullo, L., Köhler, M., et al. 2013, A&A, 558, A62
Jones, A. P., Köhler, M., Ysard, N., Bocchio, M., & Verstraete, L. 2017, A&A, 602, A46
Juvela, M. 2019, A&A, 622, A79
Kaplan, K. F., Dinerstein, H. L., Oh, H., et al. 2017, ApJ, 838, 152
Kaplan, K. F., Dinerstein, H. L., Kim, H., & Jaffe, D. T. 2021, ApJ, 919, 27
Kaufman, M. J., Wolfire, M. G., & Hollenbach, D. J. 2006, ApJ, 644, 283
Kłos, J., Lique, F., & Alexander, M. H. 2007, Chem. Phys. Lett., 445, 12

Kristensen, L. E., van Dishoeck, E. F., Mottram, J. C., et al. 2017, A&A, 605, A93

Le Petit, F., Nehmé, C., Le Bourlot, J., & Roueff, E. 2006, ApJ, 164, 506

Liu, X., Lin, J. J., Harich, S., Schatz, G. C., & Yang, X. 2000, Science, 289, 1536

Luhman, M. L., Jaffe, D. T., Keller, L. D., & Pak, S. 1994, ApJ, 436, L185

Maiti, B., & Schatz, G. C. 2003, J. Chem. Phys., 119, 12360

Marconi, A., Testi, L., Natta, A., & Walmsley, C. M. 1998, A&A, 330, 696

Mathis, J. S., Mezger, P. G., & Panagia, N. 1983, A&A, 500, 259

Nagy, Z., Choi, Y., Ossenkopf-Okada, V., et al. 2017, A&A, 599, A22

Najita, J. R., Carr, J. S., Strom, S. E., et al. 2010, ApJ, 712, 274

Offer, A. R., van Hemert, M. C., & van Dishoeck, E. F. 1994, J. Chem. Phys., 100, 362

Pabst, C. H. M., Goicoechea, J. R., Teyssier, D., et al. 2020, A&A, 639, A2

Parikka, A., Habart, E., Bernard-Salas, J., et al. 2017, A&A, 599, A20

Parikka, A., Habart, E., Bernard-Salas, J., Köhler, M., & Abergel, A. 2018, A&A, 617, A77

Parmar, P. S., Lacy, J. H., & Achtermann, J. M. 1991, ApJ, 372, L25

Pellegrini, E. W., Baldwin, J. A., Ferland, G. J., Shaw, G., & Heathcote, S. 2009, ApJ, 693, 285

Pilleri, P., Montillaud, J., Berné, O., & Joblin, C. 2012, A&A, 542, A69

Putaud, T., Michaut, X., Le Petit, F., Roueff, E., & Lis, D. C. 2019, A&A, 632, A8

Röllig, M., Abel, N. P., Bell, T., et al. 2007, A&A, 467, 187

Schirmer, T., Abergel, A., Verstraete, L., et al. 2020, A&A, 639, A144

Schirmer, T., Ysard, N., Habart, E., et al. 2022, A&A, 666, A49

Sheffer, Y., Wolfire, M. G., Hollenbach, D. J., Kaufman, M. J., & Cordier, M. 2011, ApJ, 741, 45

Sternberg, A., & Dalgarno, A. 1995, ApJS, 99, 565

Stutzki, J., & Guesten, R. 1990, ApJ, 356, 513

Tabone, B., van Hemert, M. C., van Dishoeck, E. F., & Black, J. H. 2021, A&A, 650, A192

Tappe, A., Lada, C. J., Black, J. H., & Muench, A. A. 2008, ApJ, 680, L117

Tappe, A., Forbrich, J., Martín, S., Yuan, Y., & Lada, C. J. 2012, ApJ, 751, 9

Tauber, J. A., Tielens, A. G. G. M., Meixner, M., & Goldsmith, P. F. 1994, ApJ, 422, 136

Tielens, A. G. G. M. 1993, in Dust and Chemistry in Astronomy, eds. T. J. Millar, & D. A. Williams (Routledge), 103

Tielens, A. G. G. M., & Hollenbach, D. 1985a, ApJ, 291, 722

Tielens, A. G. G. M., & Hollenbach, D. 1985b, ApJ, 291, 747

Truong, T. N. 1995, J. Chem. Phys., 102, 5335

van der Werf, P. P., Stutzki, J., Sternberg, A., & Krabbe, A. 1996, A&A, 313, 633

van Dishoeck, E. F., & Black, J. H. 1986, ApJS, 62, 109

van Dishoeck, E. F., Herbst, E., & Neufeld, D. A. 2013, Chem. Rev., 113, 9043

van Dishoeck, E. F., Kristensen, L. E., Mottram, J. C., et al. 2021, A&A, 648, A24

van Harrevelt, R., & van Hemert, M. C. 2000, J. Chem. Phys., 112, 5787

van Harrevelt, R., & van Hemert, M. C. 2001, J. Chem. Phys., 114, 9453

Veselinova, A., Agúndez, M., Goicoechea, J. R., et al. 2021, A&A, 648, A76

Visser, R., Geers, V. C., Dullemond, C. P., et al. 2007, in Molecules in Space and Laboratory, eds. J. L. Lemaire, & F. Combes (S. Diana), 102

Walmsley, C. M., Natta, A., Oliva, E., & Testi, L. 2000, A&A, 364, 301

Weck, P. F., Balakrishnan, N., Brandão, J., Rosa, C., & Wang, W. 2006, J. Chem. Phys., 124, 074308

Woitke, P., Kamp, I., & Thi, W. F. 2009, A&A, 501, 383

Wolfire, M. G., Vallini, L., & Chevance, M. 2022, ARA&A, 60, 247

Wrathmall, S. A., & Flower, D. R. 2007, J. Phys. B At. Mol. Phys., 40, 3221

Zellner, R., & Steinert, W. 1981, Chem. Phys. Lett., 81, 568

Zhang, D. H., & Zhang, J. Z. H. 1994, J. Chem. Phys., 100, 2697

Zhang, Z. E., Cummings, S. J., Wan, Y., Yang, B., & Stancil, P. C. 2021, ApJ, 912, 116

Appendix A: H$_2$O Chemistry

Appendix A.1: Neutral–neutral reactions

In the warm region, at low A_V ($A_V \leq 1$), H$_2$O is formed via neutral–neutral reactions:

$$O \underset{\text{UV}}{\overset{\text{H}_2}{\rightleftarrows}} OH \underset{\text{UV}}{\overset{\text{H}_2}{\rightleftarrows}} H_2O \cdot \tag{A.1}$$

Assuming that the abundance of total oxygen ($x_0 \simeq 3.19 \times 10^{-4}$) is the sum of the abundance of atomic oxygen, water, and hydroxyl, we get a steady-state abundance of H$_2$O of:

$$x(H_2O) = \frac{x_O}{1 + \frac{k_{\phi_1}k_{\phi_2}}{k_1 k_2 x(H_2)^2}\left(\frac{G_0}{n_H}\right)^2 + \frac{k_{\phi_2}}{k_2 x(H_2)}\left(\frac{G_0}{n_H}\right)} \, . \tag{A.2}$$

The rate coefficients used in this formula are presented Table A.1. In the Appendix, we use the thermal rates from Agúndez et al. (2010) and Veselinova et al. (2021). This formula is a generalization of that provided by Kristensen et al. (2017) (see also van Dishoeck et al. 2021) and shows that H$_2$O abundance in warm and dense environments depends primarily on G_0/n_H, T_K, and H$_2$ abundance.
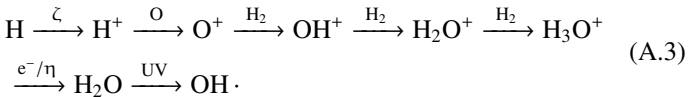
The abundance is displayed in Fig. A.1 as a function of G_0/n_H for different temperatures. The abundance increases dramatically with temperature in the $T_K = 400\text{–}1000$ K range whereas it is inversely proportional to G_0/n_H. This shows that a small change in the temperature results in a large variation in H$_2$O abundance and therefore in OH MIR emission, whereas a change in incident UV radiation field has a somewhat smaller impact.

We also show in Fig. A.3 that our analytical model nicely reproduces the abundance profile computed by the Meudon PDR code, confirming that, in the case of H$_2$ + O reactions, thermal reaction rates can be use to analyze, at least qualitatively, the affects of the physical conditions on the amount of H$_2$O and therefore on OH MIR emission.

We note that in this Appendix, we only use the thermal coefficient rate assuming H$_2$ levels follow a Boltzmann distribution. H$_2$ level distribution can be different in PDRs, in particular due to UV pumping. However, using the state-specific chemistry from Veselinova et al. (2021) only increases the abundance of H$_2$O by a factor 2.

Appendix A.2: Ion–neutral reactions

In colder regions, at higher A_V ($A_V \geq 1$), H$_2$O is formed via ion–neutral reactions. In atomic regions, the ion–neutral route is:

$$H \xrightarrow{\zeta} H^+ \xrightarrow{O} O^+ \xrightarrow{H_2} OH^+ \xrightarrow{H_2} H_2O^+ \xrightarrow{H_2} H_3O^+$$
$$\xrightarrow{e^-/\eta} H_2O \xrightarrow{UV} OH \cdot \tag{A.3}$$

where ζ is the cosmic-ray ionisation rate and η is the branching ratio of the electronic recombination forming H$_2$O ($\eta \sim 20$ %). Indeed, the electronic recombination of H$_3$O$^+$ can also lead to OH. We further assume that this series of reactions leading to H$_3$O$^+$ has an efficiency ϵ ($\epsilon \sim 15\%$):

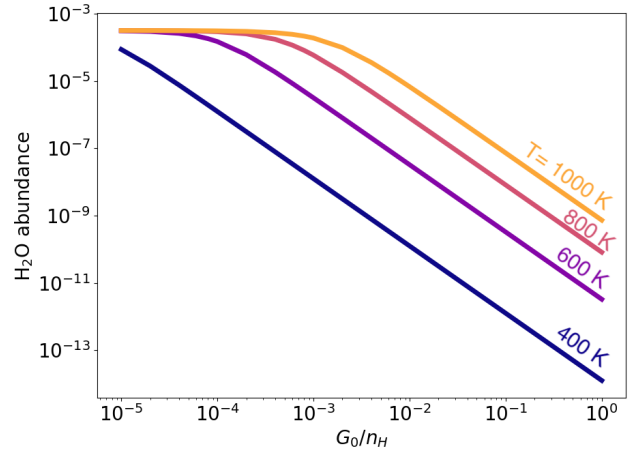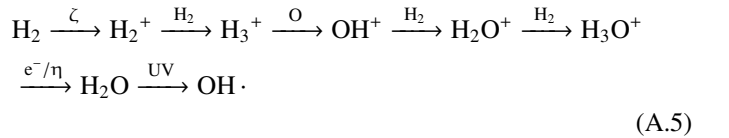$$x(H_2O) = \epsilon\eta\frac{\zeta}{k_{\phi_2}G_0}x(H). \tag{A.4}$$

Fig. A.1: H$_2$O abundance from the neutral–neutral reactions as a function of $G_0^{\text{incident}}/n_H$ for different temperatures.

In molecular regions, the ion–neutral route is slightly different:

$$H_2 \xrightarrow{\zeta} H_2^+ \xrightarrow{H_2} H_3^+ \xrightarrow{O} OH^+ \xrightarrow{H_2} H_2O^+ \xrightarrow{H_2} H_3O^+$$
$$\xrightarrow{e^-/\eta} H_2O \xrightarrow{UV} OH \cdot \tag{A.5}$$

Thus in molecular regions, we have:

$$x(H_2O) = \epsilon\eta\frac{\zeta}{k_{\phi_2}G_0}x(H_2). \tag{A.6}$$

In Fig. A.3, we show that this analytical formula nicely reproduces the abundance profile of H$_2$O in the cold and shielded region of the PDR where the neutral–neutral formation route is inefficient. However, as mentioned in Sect. 2.1, only gas-phase chemistry is taken into account in the Meudon PDR code for water formation. In those regions, formation of solid H$_2$O and subsequent photo-desorption back to the gas phase may alter the position and amplitude of the peak (Hollenbach et al. 2009; Putaud et al. 2019).

Appendix B: OH chemistry

Figure B.1 displays the different formation routes of OH; in most of the cloud, the neutral–neutral reactions can be seen to dominate. There is a significant contribution of H$_2$O photodissociation at the OH abundance peak.

Reaction	Reaction rate	Reaction rate coefficient
$O + H_2 = OH + H$	$v_1 = k_1 n(O)n(H_2)$	$k_1 = 2.22 \times 10^{-14} \times \left(\frac{T}{300}\right)^{3.75} \times \exp(-2401/T)$
$OH + H_2 = H_2O + H$	$v_2 = k_2 n(OH)n(H_2)$	$k_2 = 2.22 \times 10^{-12} \times \left(\frac{T}{300}\right)^{1.43} \times \exp(-1751/T)$
$OH + photon = O + H$	$v_{\phi_1} = k_{\phi_1} G_0 n(OH)$	$k_{\phi_1} = 1.32 \times 10^{-10}$
$H_2O + photon = OH + H$	$v_{\phi_2} = k_{\phi_2} G_0 n(H_2O)$	$k_{\phi_2} = 2.09 \times 10^{-10}$

Table A.1: Thermal rate coefficient for chemical reactions for $O+H_2$ (Veselinova et al. 2021) and $OH+H_2$ (Agúndez et al. 2010), and the photodissociation rate of OH and H_2O Heays et al. (2017).
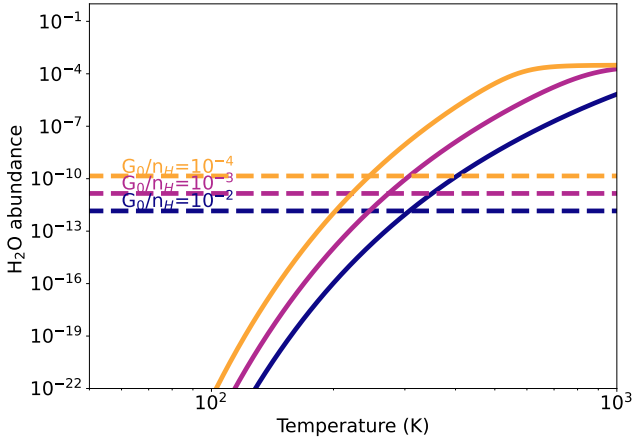

Fig. A.2: H_2O abundance as a function of temperature for different values of G_0/n_H. The dashed lines are the abundances calculated for the ion–neutral route and the solid lines are the abundances calculated for the neutral–neutral route. This figure highlights the transition temperature between ion–neutral and neutral–neutral routes.
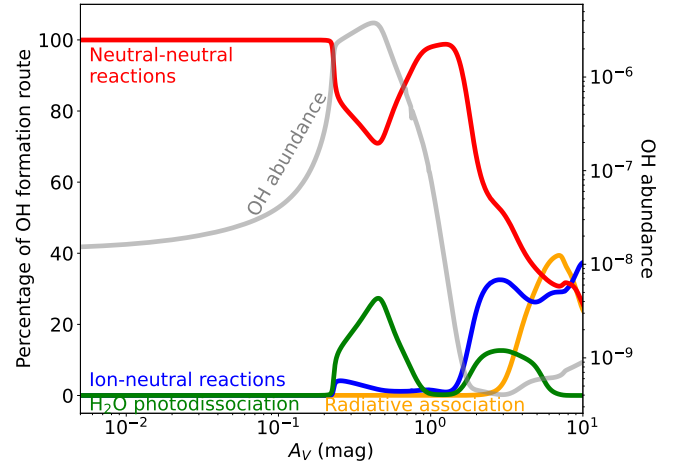

Fig. B.1: Percentage of the different formation routes of OH as a function of the visual extinction for the model $P_{th}/k = 10^8$ K cm^{-3} and $G_0^{incident} = 10^4$. The blue line represents the percentage of the ion–neutral formation route, and the red line represents the percentage of the neutral–neutral formation route, which requires high temperatures ($T_K \gtrsim 300$ K). The green line represents the percentage of the formation of OH via H_2O photodissociation. The orange line represents the percentage of the formation of OH via radiative association.
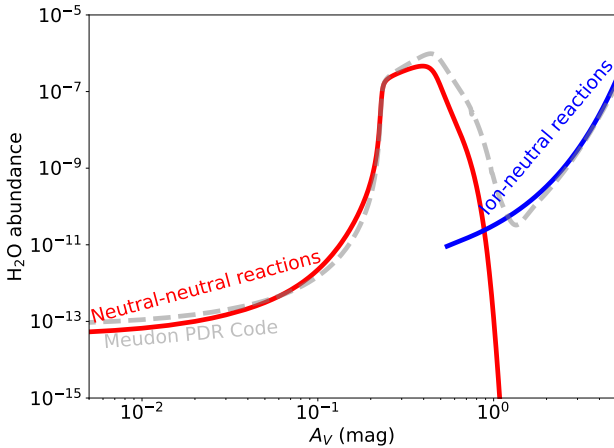

Fig. A.3: Comparison between the Meudon PDR code for a model at $P_{th}/k = 10^8$ K cm^{-3} and $G_0^{incident} = 10^4$ and the analytic calculation of H_2O abundance. The difference between the model and the analytic calculation is due to the fact we do not take into account other formation processes.